

Hybrid aerial and aquatic locomotion in an at-scale robotic insect

Yufeng Chen, E. Farrell Helbling, Nick Gravish, Kevin Ma, and Robert J. Wood

Abstract—Here we present a suite of theoretical, computational, and experimental studies culminating in the first aerial and aquatic capable insect-scale robot. We develop a computational fluid dynamics (CFD) simulation to model fluid-wing interaction in air and water. From CFD and a system dynamics analysis we predict that a multi-modal flapping strategy will enable locomotion in both air and water for a single device. We validate the CFD predictions by running at-scale, robotic wing-flapping experiments. Finally, we demonstrate for the first time a flying and swimming capable flapping-wing insect-like robot.

I. INTRODUCTION

Mobile robots capable of locomotion through complex environments are becoming increasingly essential for search-and-rescue, surveillance, and environment exploration applications [1]. Aerial vehicles [2], [3] are attractive for these applications because they can survey large area and bypass heterogeneous ground with ease. However, unlike ground-based robots that have been shown to be able to move across rough terrain and within water [4], current aerial robots are incapable of multi-modal locomotion through air and water which limits their utility [5].

The concept of dual aerial, aquatic vehicles emerged in 1939 when Russian engineer Boris Ushakov proposed the “flying submarine” [6]. In recent years, several fixed-wing dual aerial, aquatic testing platforms have been developed [7], [8]. However, designs that rely on traditional airfoils to generate lift and rotary propellers to generate thrust have been unsuccessful in achieving aquatic and aerial motion. The difference in density between air and water (1.2 kg/m^3 and 1000 kg/m^3 , respectively) poses challenges to choosing suitable wing size, vehicle cruise speed, and propeller speed. While underwater vehicle designs aim to minimize surface area to reduce drag, aerial vehicle designs need large airfoils to maintain lift. This design conflict, in addition to the reduction of rotary motor efficiency at small scales, makes fixed wing designs ineffective for hybrid aerial, aquatic micro-vehicles.

There are a number of biological examples for hybrid aerial and aquatic locomotion including a number of fish, birds, and insect species [9], [10], [11]. In particular, puffins and guillemots [10] are aquatic birds that both fly and swim by flapping-wings with adaptive kinematics for air and water.

To achieve multi-modal locomotion in a flapping-wing vehicle, wing kinematics must be adapted based on the fluid

These authors are with the School of Engineering and Applied Sciences, Harvard University, Cambridge, MA 02138, USA, and the Wyss Institute for Biologically Inspired Engineering, Harvard University, Boston, MA, 02115, USA (email: yufengchen,ehelbling, gravish, kevinma,rjwood@seas.harvard.edu)

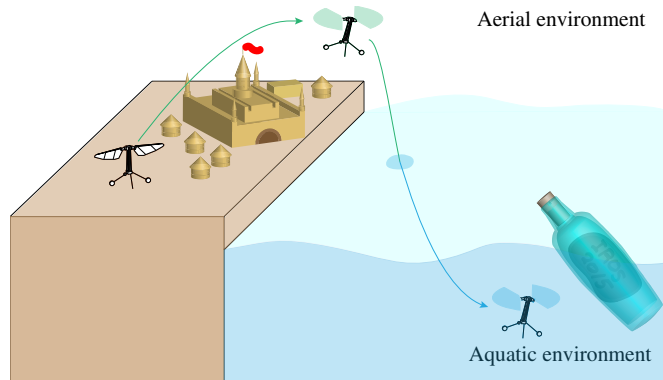


Fig. 1. The Harvard RoboBee is an **80 mg** flapping-wing aerial micro-robot. The flapping-wing design makes the robot a potential dual aerial, aquatic vehicle that varies flapping strategies in different fluid media. This conceptual illustration shows a RoboBee inspecting an buoyant object by flying in air, swimming in water, and making transitions between the fluids.

mechanics and system dynamics within these environments due to changes in fluid density and viscosity. For instance, lift-enhancing, unsteady mechanisms such as the development and shedding of the leading edge vortex (LEV) change with varying Reynolds number. While many previous studies explored these effects using dynamically scaled models [12], these experiments do not allow simultaneous inertia matching to investigate system dynamics or wing flexibility in water and air. Hence, to develop design principles for robotic aerial and aquatic locomotion, it is necessary to develop a theoretical and experimental basis of flapping-wing fluid-mechanics in these environments. Fig. 1 shows a conceptual illustration of multi-modal locomotion in which robots can land on ground and sample the environment, fly across complex terrain, and swim within water.

The Harvard RoboBee, shown in Fig. 2a, is an under-actuated flapping-wing micro-aerial vehicle that is potentially capable of both aquatic and aerial locomotion. The robot utilizes bimorph piezoelectric actuators to actively control the wing stroke motion, while the wing pitch motion is passively mediated by a polyimide flexure (Fig. 2c). Previous work on aerodynamic modeling [12], [13] and control algorithms [2] have lead to successful hovering and a number of trajectory following maneuvers in air.

Here we study flapping flight in air and water using numerical models and fluid mechanics experiments culminating in the first demonstration of a flight and swim capable flapping-wing robot. We first give a high-level scaling analysis to estimate the appropriate operating frequency and flapping amplitude that lead to suitable passive wing kinematics in

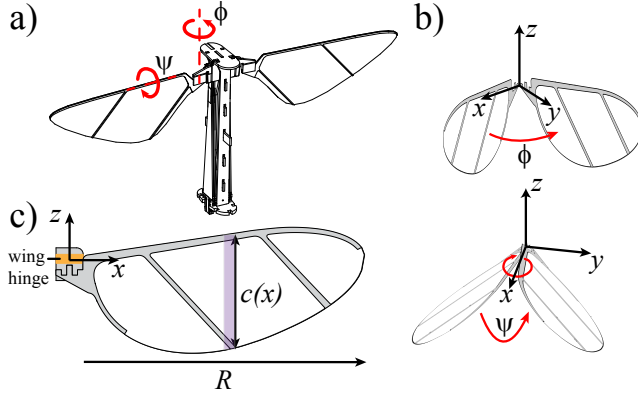


Fig. 2. RoboBee geometrical and kinematic parameters. a) Stroke angle ϕ and pitch angle ψ relative to the robot. b) ϕ rotates with respect to the z -axis and ψ rotates with respect to the x -axis. c) The wing planform used for experiments and simulations. The wing span is defined by R and wing chord $c(x)$ varies along the wing span direction. The compliant flexure position defines the coordinate system origin.

both fluids. To fully quantify the passive wing-fluid interaction in air and in water, we introduce a three dimensional computational fluid dynamics model (3D-CFD) to study the effects of decreasing Reynolds number and changing kinematics. Aquatic flapping experiments are performed to assess model accuracy and we observe excellent agreement. Based on the computational results, we find a flapping strategy for the RoboBee and demonstrate open loop swimming.

II. FLUID MODELING AND VEHICLE DYNAMICS

A. Flapping Kinematics

While insect wing kinematics have three degrees of freedom (DOF) during hover [15], stroke plane deviation is usually negligible compared to in-plane stroke motions and spanwise pitching. Consequently, most flapping-wing robots employ two rotational DOF to reduce system complexity. The RoboBee utilizes this design and its flapping kinematics are shown in Fig. 2a. As illustrated in Fig. 2b, the rotation with respect to the positive z -axis is defined as the stroke motion ϕ . The amplitude and frequency of stroke motion are fully controlled by a piezoelectric actuator. The second DOF, ψ , is defined with respect to the negative x -axis and is passively controlled by a compliant flexure. Fig. 2c shows the flexure position, the wing planform, and labels local chord length $c(x)$ and wing span R .

When the actuators are driven with a sinusoidal input around 100 – 140 Hz in air, the measured pitch motion closely resembles a phase shifted sinusoid. Fig. 3 illustrates a typical flap cycle. Analytically, the wing stroke and pitch kinematics can be written as

$$\begin{aligned}\phi(t) &= \phi_{max} \cos(2\pi ft) \\ \psi(t) &= -\psi_{max} \sin(2\pi ft - \delta),\end{aligned}\quad (1)$$

where ϕ_{max} is the stroke amplitude, ψ_{max} is the pitch amplitude, f is the flapping frequency and δ is the relative phase.

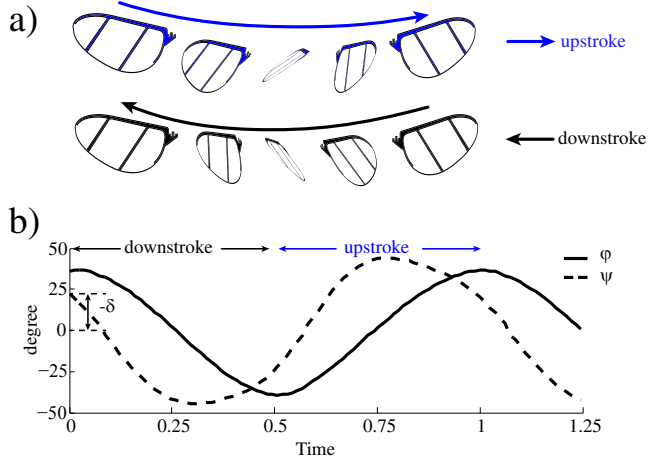


Fig. 3. RoboBee flapping kinematics. a) Upstroke and downstroke of a typical flapping period. Wing stroke ϕ is actively controlled and pitch ψ is passive. b) Experimentally measured $\phi(t)$ and $\psi(t)$. These functions can be fit to equation (1). The time scale is normalized to one flapping period.

B. Scaling analysis

We identify the frequency range at which a flapping-wing aerial robot can operate in an aquatic environment using the quasi-steady formula:

$$\bar{F}_L = \frac{1}{2} \bar{C}_L \rho U_{rms}^2 S, \quad (2)$$

where \bar{F}_L is mean lift force, \bar{C}_L is the time averaged lift coefficient, ρ is the fluid density, U_{rms} is the root mean square of wing tip velocity, and S is the wing surface area. Since the wing planform, inertia, and hinge stiffness are unchanged as the vehicle transitions from air to water, we need to change input frequency and stroke amplitude to maintain the desired mean lift forces. Invoking equation (2) leads to

$$\rho_{air}(\phi_{max,air} R f_{air})^2 = \rho_{water}(\phi_{max,water} R f_{water})^2, \quad (3)$$

For an under-actuated flapping-wing aerial robot like the RoboBee, ϕ_{max} is actively controlled by vehicle actuation. If ϕ_{max} is chosen to remain constant, then the flapping frequency in water can be estimated as:

$$f_{water} = \sqrt{\frac{\rho_{air}}{\rho_{water}}} f_{air} \quad (4)$$

The quasi-steady model also gives estimate of the fluid power dissipation in air and water:

$$\bar{P} = \bar{F} \cdot U_{rms} \cong \frac{1}{2} \bar{C}_L \rho U_{rms}^3 S \quad (5)$$

Substituting equation (4) into equation (5) suggests that fluid power dissipation ratio in air and water is inversely proportional to the square root of the fluid density ratio:

$$\frac{P_{air}}{P_{water}} \cong \sqrt{\frac{\rho_{water}}{\rho_{air}}} \quad (6)$$

C. Numerical model with fully prescribed kinematics

The scaling analysis of equation (2) does not consider the Reynolds number of the fluid-wing interaction. Reynolds number is an important factor for flapping-wing flight and is the ratio of inertial to viscous forces:

$$Re = \frac{U_{rms}R}{\nu}, \quad (7)$$

where ν is the kinematic viscosity of the immersed fluid. As shown in a previous study [14], changes in passive pitching can lead to over 70% change in mean lift generation. Hence, it is important to model these unsteady effects using high fidelity computational solvers.

We implement a CFD model that solves the three dimensional incompressible Navier Stokes equation:

$$\begin{aligned} \frac{\partial \mathbf{u}}{\partial t} + \mathbf{u} \cdot \nabla \mathbf{u} &= -\frac{1}{\rho} \nabla p + \nu \nabla^2 \mathbf{u} \\ \nabla \cdot \mathbf{u} &= 0 \end{aligned} \quad (8)$$

where $\mathbf{u} = (u, v, w)$ is the fluid velocity field and p is the pressure field. We further impose a non-slip boundary condition for the velocity field along the wing surface and a far field pressure boundary condition:

$$\begin{aligned} \mathbf{u}|_{wing} &= (u, v, w)|_{wing} \\ p|_{\infty} &= 0 \end{aligned} \quad (9)$$

The Reynolds number, in the non-dimensionalized form of equation (8), can be interpreted as the ratio between inertial and viscous force contribution, which affects vortex growth and consequently force generation.

We implement the numerical solver using the nodal discontinuous Galerkin finite element method on a moving Cartesian coordinate system. The wing planform and the chord-wise cross section are modeled as thin ellipses. Fig. 4 shows an illustration of the wing surface mesh, the inertial coordinate system (x, y, z) and the moving coordinate system (ξ, η, ζ). The computational mesh is generated from the open source package gmsh [16]. The solver uses first-order Lagrange polynomials as the interpolation basis for each tetrahedral element. The Navier Stokes solver is based on a multi-step method introduced in [17]. A first-order limiter based on [18] is implemented to remove artificial numerical oscillations. Finally, given solutions to the flow fields, the instantaneous force and torque with respect to wing root are computed by numerically integrating over the shear stress tensor:

$$\begin{aligned} \mathbf{F} &= \int_{wing} \mathbf{n} \cdot \boldsymbol{\sigma} da, \\ \mathbf{T} &= \int_{wing} \mathbf{r} \times (\mathbf{n} \cdot \boldsymbol{\sigma}) da \end{aligned} \quad (10)$$

where $\boldsymbol{\sigma} = -p\mathbf{I} + \mu(\nabla \mathbf{u} + \nabla \mathbf{u}^T)$ is the shear stress tensor, \mathbf{r} is the displacement from wing root and \mathbf{n} is the local wing surface normal at the differential surface da . This numerical solver takes as input the prescribed flapping kinematics as time varying boundary conditions to the Navier Stokes equation.

The simulation is compared to a previous flapping experiment using measured kinematic parameters $\phi_{max} = 35^\circ$, $\psi_{max} = 43^\circ$, $\delta = 0^\circ$ and $f = 120 \text{ Hz}$. The measured

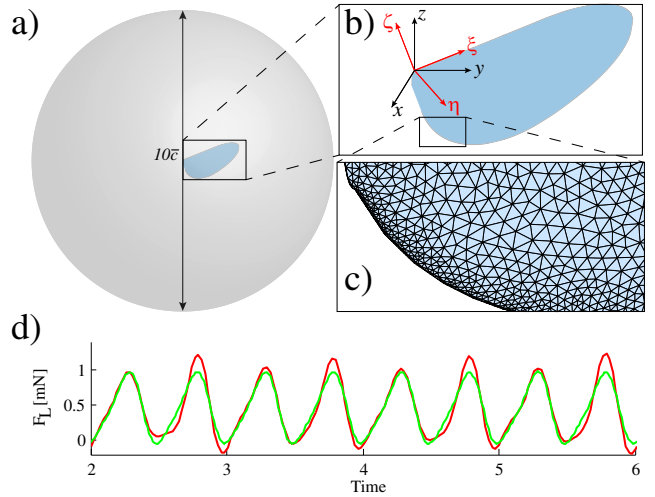


Fig. 4. Computational mesh of 3D-CFD simulations and simulation validation. a) The spherical computational domain radius is 10 times the mean wing chord. b) Definitions of the inertial coordinate system (x, y, z) and the moving coordinate system (ξ, η, ζ). Both origins are at the leading edge of the wing root. c) An enlarged view of wing surface mesh. The computational mesh consists of 140,000 tetrahedral elements and 15,000 surface elements. d) A comparison between experimentally measured lift force (red) and simulated lift force (green) using measured kinematics.

instantaneous lift force is processed using a 500 Hz low pass filter and is shown in Fig. 4d (red curve). The computed instantaneous lift force (green curve) closely matches the experimental measurement. The relative error of numerical model is 16% in this case.

D. Numerical model with passive hinge pitching

Our fully-prescribed CFD is capable of reproducing the experimentally observed aerodynamic forces on flapping wings (Fig. 4d), however many fluid-structure interactions, including the wings of the RoboBee, involve flexible elements. To study fluid-wing interaction we model the compliant flexure as a torsional spring. At each computational time step, we find the fluid torque component along the wing pitch axis. The wing pitch component of the Euler angular momentum equation $\sum \tau_i = \mathbf{I} \cdot \dot{\omega} + \mathbf{w} \times (\mathbf{I} \cdot \omega)$ can be expanded as

$$K\psi + \tau_{fluid} = -I_{xx}\ddot{\psi} - (I_{yy} - I_{zz})\dot{\phi}^2 \cos \psi \sin \psi, \quad (11)$$

where K is the wing hinge stiffness, τ_{fluid} is the fluid torque along wing pitch axis, I_{xx} , I_{yy} and I_{zz} are the wing principal moments of inertia. This second order ordinary differential equation describes the passive wing pitching motion. Solutions from the Navier Stokes equation are used to calculate fluid torque τ_{fluid} , which is the input to equation (11). $(\psi, \dot{\psi}, \ddot{\psi})$ are solutions to equation (11) and serve as inputs to equation (8). Solving this coupled ODE-PDE system allows us to study fluid-wing interaction. We give the value of K in section IIIB.

E. Vehicle dynamics and energetics

When a flapping-wing robot is placed in an aquatic environment, the vehicle's dynamics change due to increased

damping from the water. We give an analysis of the buoyancy effect, change of system resonance, cruise speed, upright stability and system energetics for the Harvard RoboBee in water.

The current RoboBee is primarily composed of piezoelectric ceramics and carbon fiber whose densities are 7 g/cm^3 and 1.6 g/cm^3 , respectively. In an aquatic environment, buoyancy accounts for less than 14% of the vehicle weight, therefore wing flapping must be the main contribution to the lift force. The robot is designed such that its aerial flapping frequency centers around the system resonance in air to achieve large wing stroke amplitudes. A previous study [19] from our group found that system resonance is well estimated using a linearized lumped parameter model. In an aquatic environment, the added mass and effective damping more than double. Consequently, the vehicle becomes over-damped and the maximum stroke amplitude reduces to around 30° at low frequencies. Thus we predict that for successful locomotion in water, we will need to drive the wings at higher frequency to account for the reduction in amplitude.

To address the swimming capabilities of RoboBee we consider fluid drag during locomotion. In an aerial lateral maneuver, the RoboBee can achieve velocities of 0.5 m/s , which is about 10% of the maximum wing stroke velocity. The aerodynamic drag on the airframe is negligible compared to forces on the wing. In water, the maximum wing stroke velocity is around 20 cm/s and this places an upper bound on the vehicle speed. Fluid drag becomes significant when vehicle speed exceeds 6.5 cm/s , at which point the drag on the airframe exceeds 70% of the thrust according to equation (2). Thus, we estimate the vehicle mobility will be limited to 10 cm/s in water.

Changes in flying kinematics and fluid density also affect vehicle upright stability. Compared to aerial flight, the robot flaps at a reduced frequency but produces equivalent fluid forces and torques. Consequently, the amplitude of the body oscillation is magnified by the ratio of flapping frequencies in air and water—approximately 15—during open loop take off or low speed swimming ($< 1\text{ cm/s}$). On the contrary, fluid torque acting on the robot’s airframe enhances upright stability at high vehicle speed ($> 5\text{ cm/s}$) because the robot geometric center is designed to be higher than the center of mass. This analysis is supported by the observation that the RoboBee remains upright during free fall in water.

The scaling analysis in Section II compares fluid power dissipation in air and water. The robot efficiency also depends on the loss from the piezo-bending actuators and transmission flexures. The piezoelectric actuators are modelled as capacitive plates and the power efficiency is proportional to operating frequency. The robot transmission efficiency is similar in air and water because frictional loss in compliant flexures is negligible. Compared to hovering flight in air, flapping locomotion in water costs less fluid dissipation but has lower actuator efficiency. Experimental comparison of total power usage in air and water is given in Section IV.

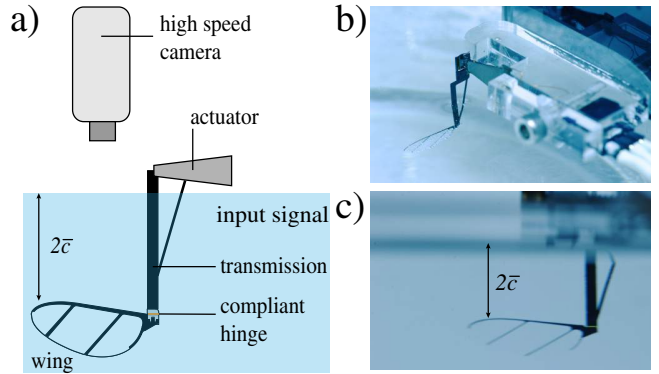


Fig. 5. Experimental setup in water. a) Schematic of the actuator, transmission, compliant flexure, and wing assembly. A high speed video camera is positioned overhead to record the flapping kinematics. b) and c) The perspective and anterior view of the flapping-wing setup. The wing leading edge is placed at a distance $2\bar{c}$ below the water surface to avoid surface effects. The wing planforms in a) and c) are identical however there is some optical distortion when the wing is placed in a cylindrical beaker.

III. EXPERIMENT SETUP

To validate the scaling analysis and numerical models, we perform flapping experiments in air and water using the same actuator, wing, and wing hinge. For aerial flapping experiments, we use an existing setup [12] for motion tracking and lift measurement. For aquatic flapping experiments, we extend the wing driver transmission to fully submerge the wing. We measure input voltage and current to study the system energetics for both aerial and aquatic experiments.

A. Actuator, wing and wing hinge

The bimorph piezoelectric actuators can be driven up to 300V and 140Hz . A flexure-based transmission system converts linear actuator displacement to the angular wing stroke. Fluid forces and restoring hinge torque on the flapping-wing cause passive wing pitching. Previous studies [20] modeled the torsional stiffness as

$$K = \frac{Et^3w}{12L}, \quad (12)$$

where E is the Young’s modulus of the polyimide material, t , w , and L are flexure thickness, width, and length, respectively. In our experiments the wing hinge dimensions are $t = 7.5\mu\text{m}$, $L = 45\mu\text{m}$, and $w = 1.25\text{ mm}$. The corresponding wing hinge stiffness is estimated to be $2.4\mu\text{Nm/rad}$. The wing consists of a carbon fiber frame and polyester membrane and weighs 0.7 mg , spans 12.8 mm and has surface area 54 mm^2 . The wing morphology is chosen based on Ellington’s study on insect wing shape parametrization [15].

B. Flapping experiments in aquatic environments

As shown in Fig. 5, we operate the actuator outside of water to prevent shorting and extend the transmission such that the wing is fully submerged. The wing is driven at $3 - 6\text{ Hz}$ and the motion is recorded at 200 Hz with a Phantom V7.3 high speed camera. Wing stroke and hinge motions are extracted using a similar method developed in a previous

work [13]. The measured passive pitching is later compared with a numerical simulation that uses measured wing stroke motion as the input. We do not measure time varying forces for flapping experiments in water because of the difficulty to incorporate sensitive electronics.

IV. RESULTS

We run a series of simulations and experiments to demonstrate the feasibility of flapping locomotion in aquatic environments. 3D-CFD simulations using fully prescribed kinematics estimated from the scaling analysis are done to compare flow structures and wing dynamics in air and water. We further conduct flapping experiments in water to study passive pitching. The measured pitching kinematics are compared with 3D-CFD simulations using a partially prescribed kinematic model. In addition, we demonstrate RoboBee open-loop swimming.

A. Flapping in water versus in air

A hovering RoboBee flaps at 120 Hz in air with 70° peak to peak stroke amplitude. A previous aerial flapping experiment measured the corresponding pitching kinematic parameters to be $\psi_{max} = 43^\circ$, and $\delta \approx 0^\circ$. Assuming ϕ_{max} , ψ_{max} , and δ are identical in air and water, equation (2) predicts the hovering frequency in water to be 4.1 Hz. We further use the 3D-CFD solver to compare flapping flight in water versus air using the ϕ_{max} , ψ_{max} , δ from aerial experiments at different frequencies. Fig. 6 compares the computed lift, drag and wing hinge torque. Although the Reynolds numbers differ by 46%, we observe that these quantities are very similar between flapping in air (green) and in water (blue).

Fig. 7 illustrates the similarities between air and water velocity fields and the pressure field. We show the flow fields (U_x , U_y , U_z components) and the pressure field (PR) on a 2D plane that intersects the mid-span wing chord and when stroke velocity is at maximum ($T = 2.25$). The aerial and aquatic flapping speed at wing mid-span are approximately 2 m/s and 7 cm/s, respectively. Since water density is about 1000 times greater than air, the pressure fields in both fluid media have similar magnitudes (10 N/m²).

In the intermediate Reynolds number regime, pressure dominates viscous shear. Our simulations show that pressure accounts for over 90% of lift and drag on the wing. Fig. 8a further compares the pressure distribution on the wing surfaces when stroke velocity is at the maximum ($T = 2.25$). In both cases the upper wing surface has a negative pressure profile (blue) and the lower wing surface has a positive pressure profile (red). We use the same color scale for both aerial (left) and aquatic (right) simulations.

Although pressure contribution dominates, viscous shear is important in the unsteady boundary layer and is responsible for the growth and shedding of vortices. Fig. 8b illustrates the iso-vorticity contour on the upper wing surface. In both cases we observe the development of a LEV, a weak trailing edge vortex (TEV), and a very strong wing tip vortex.

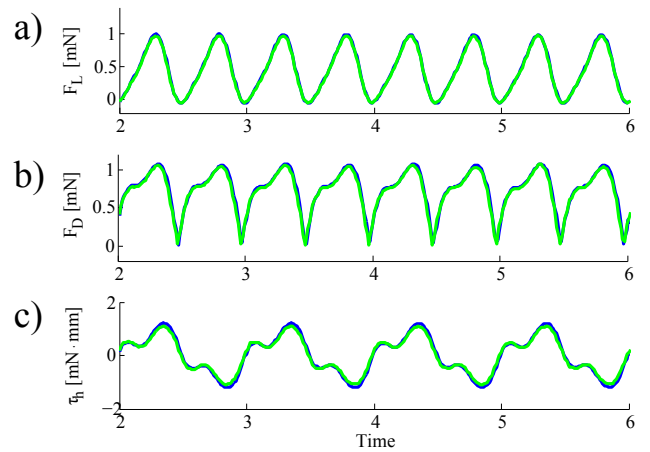


Fig. 6. Lift, drag and wing pitch torque in water and air from CFD computation. In a), b) and c) green and blue colors represent simulation for aerial flapping at 120Hz and aquatic flapping at 4.1Hz, respectively. The time scales are normalized to flapping period. We show the second to sixth flapping period to avoid initial transients. a) Instantaneous lift force comparison shows aerial and aquatic flapping generates similar lift forces. b) and c) Further comparison of simulated drag forces and wing pitch torques in air and water.

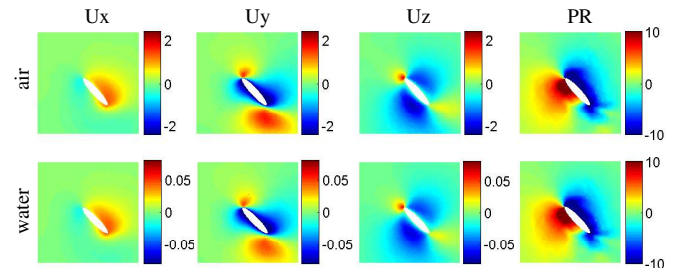


Fig. 7. Comparison of instantaneous fluid flow fields and pressure field in air and water. The top row illustrates U_x , U_y , U_z , and PR in air and the bottom row illustrates the corresponding quantities in water. We show solutions on a 2D plane that intersects wing chord near wing mid-span at $T = 2.25$. While the magnitudes of flapping velocities differ in air and water, the pressure fields are very similar due to the higher water density. The unit for U_x , U_y , U_z are m/s, and the units for PR is N/m².

The vortex structures observed in Fig. 8b explain the negative pressure profile seen on the upper wing surface (Fig. 8a). From a fluid dynamics perspective, these vortex structures represent regions of low pressure because streamline curvature implies a negative pressure gradient. Our numerical simulations show vortex structures and pressure profiles are similar for aerial and aquatic flapping locomotion at the chosen kinematics.

B. Passive pitching kinematics in water

While 3D-CFD simulations with fully prescribed flapping kinematics show that aerial and aquatic flapping locomotion share similar fluid structures and force profiles, fluid-wing interactions are ignored in previous models. We investigate passive pitching through flapping experiments in water and running coupled fluid-wing CFD simulations.

The kinematic parameter δ specifies the phase shift between wing stroke $\phi(t)$ and pitch $\psi(t)$. While flapping exper-

iments with passive pitching do not have direct control over δ , this parameter has strong influence on mean lift and drag. A previous experimental study [13] showed how negative δ corresponds to large mean lift in aerial flapping. Here we quantify the effect of δ in aquatic flapping through 3D-CFD simulations. Fig. 9a shows \bar{C}_L and \bar{C}_D as functions of δ . \bar{C}_L is a monotonically decreasing function as δ increases, which indicates aquatic flapping produces large mean lift when δ is negative. \bar{C}_D is a decreasing function for $\delta < 0^\circ$ and flattens out for $\delta > 0^\circ$. Fig. 9 also shows δ 's influence on \bar{C}_L/\bar{C}_D , which is a measure of flight endurance. We observe that maximum flapping efficiency is achieved at $\delta = -10^\circ$. A previous study of flapping-wing flight in air [21] also found advance wing rotation (negative δ) benefits lift production. This result shows the influence of the phase parameter on lift and drag forces in water is very similar to its effect in air.

Having quantified the phase effect on lift and drag generation, we further study the phase dependence on controlled input parameters ϕ_{max} and f . Flapping experiments were done in water at different frequencies and stroke amplitudes. Fig. 10 shows an experiment done at $\psi_{max} = 33^\circ$ and $f = 4.1 \text{ Hz}$, which is very similar to the stroke kinematics described in Fig. 6. Images from Fig. 10a are analyzed to extract flapping kinematics, and the measured $\phi(t)$ and $\psi(t)$ are shown as dotted lines in Fig. 10b. The measured stroke motion is approximated as a pure sinusoid and used as the input to the coupled fluid-wing CFD solver for comparison with experiments. Fig. 10b also compares the simulated and measured $\phi(t)$ and $\psi(t)$. We observe close agreement between the experiment and the simulation, and the relative error for $\phi(t)$ and $\psi(t)$ are 8% and 17%, respectively. The measured and computed phase shift δ are 3° and -1.5° , respectively.

Aside from the difference in flapping frequency, kinematic parameters ϕ_{max} and ψ_{max} are similar to the operating condition in air. The numerically computed mean lift forces are also similar. Experimentally we measure the average power drawn by the wing driver in air and water:

$$P_{total} = \frac{1}{T} \int_0^T i_{act} v_{act} dt, \quad (13)$$

where T is a flapping period, v_{act} and i_{act} are applied voltage and measured current across the actuator. For $\phi_{max} \approx 40^\circ$, $\psi_{max} \approx 35^\circ$, $f_{water} = 4.1 \text{ Hz}$, and $f_{air} = 120 \text{ Hz}$, we measure $P_{water} = 4.1 \text{ mW}$ and $P_{air} = 25.4 \text{ mW}$. This measurement shows that although the actuator efficiency is lower in water, the average power cost in water is about 6 times smaller than that of in air. This is mainly contributed by the reduction in fluid dissipation.

C. Open loop take off in water

Given positive results from the 3D-CFD and the flapping-wing experiments demonstrating that flapping-wing locomotion is feasible in an aquatic environment, we demonstrate underwater locomotion using a flapping-wing micro-aerial vehicle. The RoboBee used in these experiments is

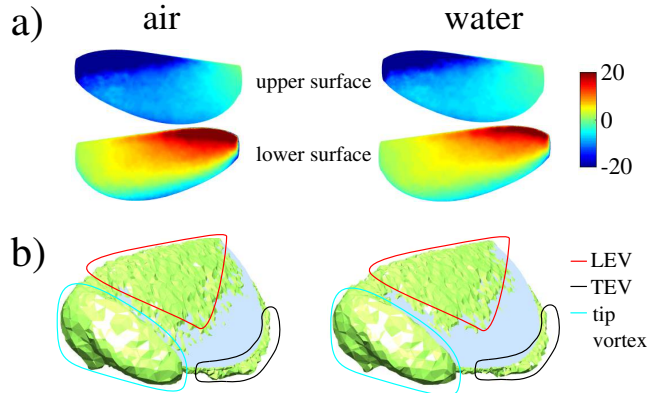


Fig. 8. Pressure distribution and vortex structures in air and water. In a) and b) left and right figures correspond to aerial and aquatic flapping, respectively. a) The pressure profile on the wing surface at $T=2.25$. The pressure profile is negative (blue) on the upper wing surface and positive (red) on the lower wing surface. All plots use the same color scale and the units is N/m^2 . b) The leading edge vortex (LEV), the trailing edge vortex (TEV), and wing tip vortex structures are similar in both cases. The values of the aerial (left) and aquatic (right) iso-vorticity contours are $1200/\text{s}$ and $41/\text{s}$, respectively. Both values normalize to 10 when the time scales are non-dimensionalized.

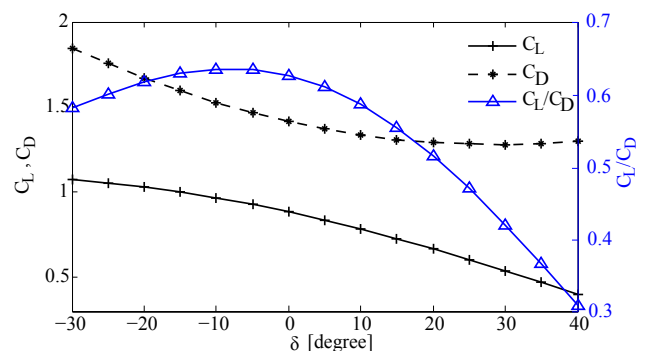


Fig. 9. Phase effect on lift and drag forces. Aquatic flapping simulations are done using $\phi_{max} = 35^\circ$, $\psi_{max} = 43^\circ$, $f = 4.1$, and $\delta \in [-30, 40]$. We compute \bar{C}_L and \bar{C}_D by taking the averaged lift and drag forces for six flapping periods and then normalizing using equation (2). The simulations show $\delta < 0^\circ$ is favorable for aquatic flapping because for $\delta \geq 0^\circ$ both \bar{C}_L and \bar{C}_L/\bar{C}_D decrease. The simulations show operating at appropriate δ is crucial for flapping efficiency.

mechanically identical to the design in [2]. We mitigated electric shorting by using deionized water and insulating the electrical connections at the base of the robot as well as along the edges of the piezo bimorph with CA glue (Loctite 416, Henkel Corporation, Ohio, USA).

We first run static tests to characterize system performance in aerial and aquatic environments. With a drive signal of 200 V , we perform a frequency sweep between $10 - 130 \text{ Hz}$ in air and $1 - 13 \text{ Hz}$ in water to find ϕ_{max} dependence on driving frequency. In an aerial environment shown in Fig. 11a, system resonance is observed to be 110 Hz . Assuming $\delta \approx 0^\circ$ which corresponds to $\bar{C}_L = 0.85$, we plot the estimated lift using equation (2) and show that maximum lift is achieved around 120 Hz . In the aquatic environment shown in Fig. 11b, the experiment confirms that the system is over-damped since ϕ_{max} decreases as

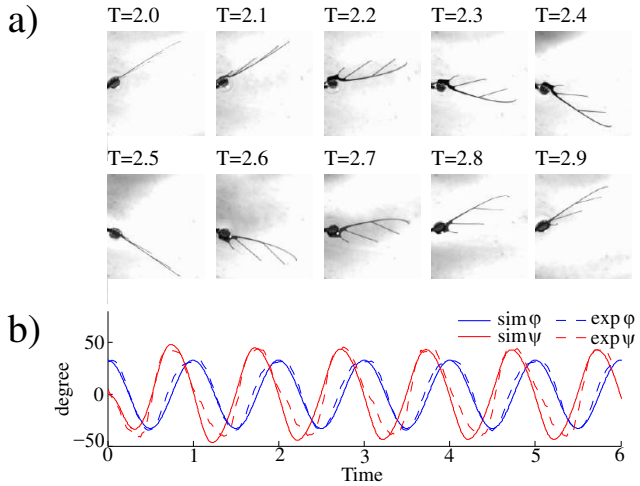


Fig. 10. Passive pitching experiments and simulations in water. a) Images of a passively pitching wing driven at $\psi_{max} = 33^\circ$, $f = 4.1\text{ Hz}$. b) Measured kinematics and simulated results. The passive hinge rotation matches very closely with experimental results.

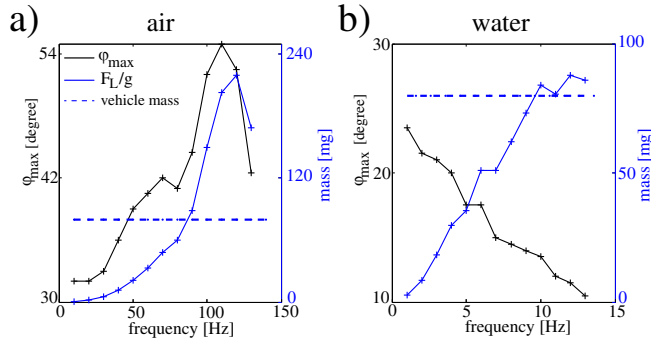


Fig. 11. System characterization in air and water. a) System resonance occurs at 110 Hz in aerial flapping experiments. b) ϕ_{max} decreases monotonically as driving frequency increases in water. The blue curves show estimated mean lift force assuming $C_L = 0.85$. The dotted lines show vehicle weight.

frequency increases. Although the wing stroke amplitude decreases, the quasi-steady model predicts increasing lift with increasing frequency in water. To generate sufficient mean lift at lower ϕ_{max} we increase flapping frequency above 4.1 Hz according to equations (2). These results were also seen during a number of open loop “flights,” and takeoff occurred at 9 Hz frequency with 28° stroke amplitude.

Torque production in water is similar to that in air. We control pitch torque by adjusting the mean stroke angle of the wings and by tuning the mean voltage of the sinusoid delivered to the actuators. Roll torques are produced by flapping the wings at differing amplitudes by varying the stroke amplitude of the two wings [2]. We ran a number of open-loop tests to validate this claim, by varying the sinusoidal signal we were able to produce both positive and negative pitch torques as well as positive and negative roll torques underwater.

Fig. 12a demonstrates a swimming RoboBee after pitch and roll offsets have been experimentally determined. The

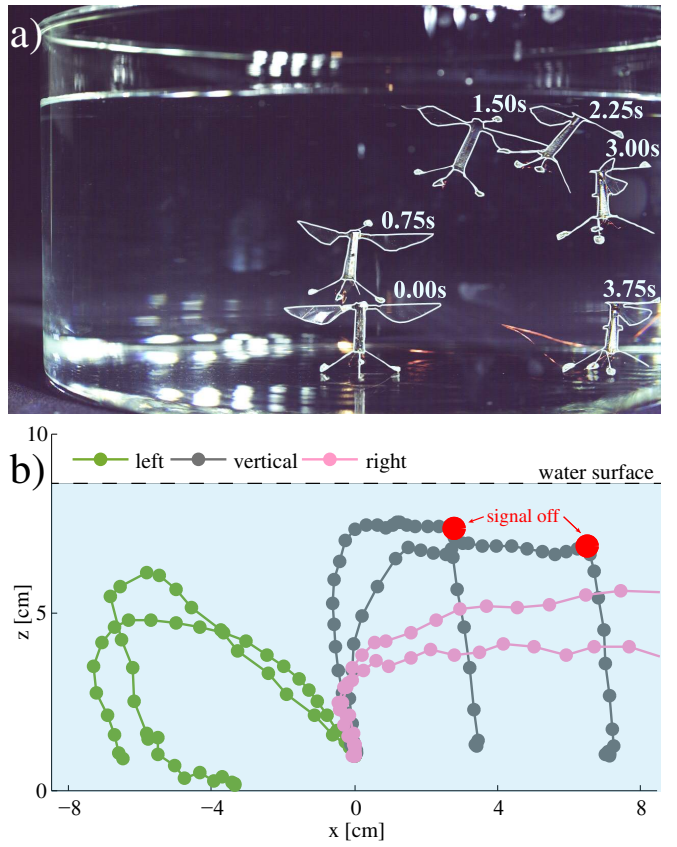


Fig. 12. RoboBee open loop take off and swimming demonstration. a) A RoboBee flaps at 9 Hz and ascends at 6 cm/sin water. The bee is turned off after it reaches the free surface. b) A number of open loop swimming trajectories. We vary input torque commands to demonstrate vertical take off, and left and right maneuvers. The blue shaded region represents the aquatic environment and shows the free water surface. The robot reaches the air-water interface in both cases of vertical take off.

RoboBee is able to takeoff and ascend to the surface of the water at a velocity of 6 cm/s where it traverses along the air-water interface until we stop the signal at $T = 2.7\text{ s}$ and the RoboBee sinks to the bottom of the dish. Fig. 12b shows six trajectories that demonstrate open loop vertical take off, left, and right maneuvers. During vertical take off experiments, the robot moves horizontally once its wings break the free water surface. The robot maintains upright stability and lands on its feet after the driving signal is turned off. A swimming demonstration is included in the supplementary video.

D. Air-water transition

In addition to demonstrating the robot’s ability to fly and swim, we give preliminary results on air-water transition. Experimentally we find that flapping wings are damaged if they hit the water surface when wing tip velocity exceeds 3 m/s . Consequently, the flapping motion needs to be commanded off during air-water transition. Swimming kinematics are switched on after the wings are fully submerged. At the insect scale we find surface tension to be a hindering factor between air-water transition. The surface tension can be estimated as $F = \gamma L$, where γ is the surface tension coefficient of water, and L is the length of the wing. The

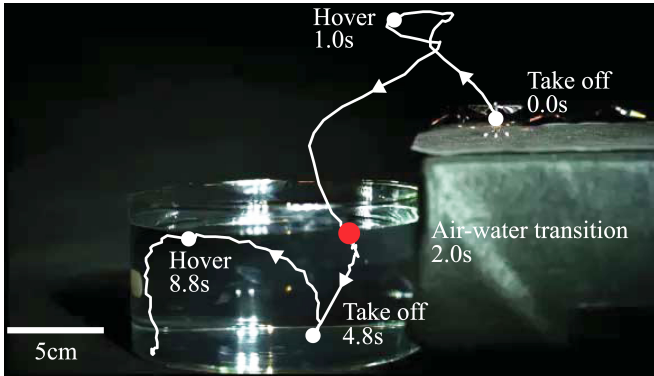


Fig. 13. Air-water transition demonstration. A RoboBee is commanded to take off from ground. It is turned off in mid-air and falls passively into water. Next, the robot is controlled open loop to swim to reach the water surface. The red dot indicates air-water transition.

surface tension is 160 mg and exceeds the robot weight. We resolve this problem by coating the RoboBee wing with liquid detergent, which dissolves in water and significantly reduces the surface tension. This technique allows successful air-water transition. Figure 13 shows an air-water transition demonstration. We leave water-air transition studies to future work.

V. CONCLUSION AND FUTURE WORK

Flapping propulsion is a feasible aquatic locomotion strategy for an insect-scale micro-aerial vehicle. By comparing flapping flight in air and in water through 3D-CFD simulations and experiments, we found that favorable passive pitching can be obtained in both water and air using the identical wing hinge design. Further, we demonstrated open-loop swimming in an aquatic environment with the RoboBee.

Bio-inspired flapping provides a creative solution to the long established challenge of designing hybrid aerial and aquatic vehicles. In our study of flapping-wing locomotion in air and water, the fluid dynamical analysis is not limited to insect-scaled vehicles. From millimeter scaled insects to meter scaled fish and birds, flapping-wing locomotion observed in biology spans a large range of animal size and weight. This suggests the locomotion strategy has the potential to be adapted to larger hybrid aerial, aquatic robotic designs.

We believe the RoboBee has the potential to become the world's first successful dual aerial, aquatic insect-scale vehicle. While previous work [2] and this paper demonstrate the robot's ability to fly, swim, and make air-water transitions, in future studies we need to demonstrate water-air transition by developing new control strategies.

VI. ACKNOWLEDGMENT

This material is based upon work supported by the National Science Foundation Graduate Research Fellowship under Grant No. (DGE1144152), and the Wyss Institute for Biologically Inspired Engineering. Any opinions, findings, and conclusions or recommendations expressed in this material are those of the authors and do not necessarily

reflect the views of the National Science Foundation. NG was supported by a James S. McDonnell post-doctoral fellowship. The computations in this paper were run on the Odyssey cluster supported by the FAS Division of Science, Research Computing Group at Harvard University.

REFERENCES

- [1] Chung, Timothy H., Geoffrey A. Hollinger, and Volkan Isler. "Search and pursuit-evasion in mobile robotics." *Autonomous robots* 31.4 (2011): 299-316.
- [2] K. Ma, P. Chirarattanon, S. Fuller, and R.J. Wood, "Controlled Flight of a Biologically Inspired, Insect-Scale Robot", *Science*, vol. 340, pp. 603-607, 2013.
- [3] Lentink, David, Stefan R. Jongerius, and Nancy L. Bradshaw. "The scalable design of flapping micro-air vehicles inspired by insect flight." In *Flying Insects and Robots*, pp. 185-205. Springer Berlin Heidelberg, 2010.
- [4] Crespi, Alessandro, and Auke Jan Ijspeert. "AmphiBot II: An amphibious snake robot that crawls and swims using a central pattern generator." *Proceedings of the 9th international conference on climbing and walking robots (CLAWAR 2006)*. No. BIOROB-CONF-2006-001. 2006.
- [5] Siddall, R., and M. Kovač. "Launching the AquaMAV: bioinspired design for aerial-aquatic robotic platforms." *Bioinspiration & biomimetics* 9.3 (2014): 031001.
- [6] D.V. Reid, "Flying submarine", U.S. Patent, June 4, 1963, 3092060
- [7] Liang, Jianhong, et al. "Design and Experiment of a Bionic Gannet for Plunge-Diving." *Journal of Bionic Engineering* 10.3 (2013): 282-291.
- [8] Fabian, Andrew, et al. "Hybrid Aerial Underwater Vehicle (MIT Lincoln Lab)." (2012).
- [9] Davenport, John. "How and why do flying fish fly?." *Reviews in Fish Biology and Fisheries* 4.2 (1994): 184-214.
- [10] Lock, Richard J., et al. "Development of a biologically inspired multi-modal wing model for aerial-aquatic robotic vehicles through empirical and numerical modelling of the common guillemot, Uria aalge." *Bioinspiration & biomimetics* 5.4 (2010): 046001.
- [11] SUDO, Seiichi, et al. "Swimming behavior of small diving beetles." *Journal of Advanced Science* 18.1/2 (2006): 46-49.
- [12] Dickinson, Michael H., Fritz-Olaf Lehmann, and Sanjay P. Sane. "Wing rotation and the aerodynamic basis of insect flight." *Science* 284.5422 (1999): 1954-1960.
- [13] Desbiens, Alexis Lussier, Yufeng Chen, and Robert J. Wood. "A wing characterization method for flapping-wing robotic insects." *Intelligent Robots and Systems (IROS), 2013 IEEE/RSJ International Conference on*. IEEE, 2013.
- [14] Chen, Yufeng, Alexis Lussier Desbiens, and Robert J. Wood. "A computational tool to improve flapping efficiency of robotic insects." *Robotics and Automation (ICRA), 2014 IEEE International Conference on*. IEEE, 2014.
- [15] Ellington, C. P. "The aerodynamics of hovering insect flight. I. The quasi-steady analysis." *Philosophical Transactions of the Royal Society of London. B, Biological Sciences* 305.1122 (1984): 1-15.
- [16] C. Geuzaine and J.-F. Remacle. Gmsh: a three-dimensional finite element mesh generator with built-in pre- and post-processing facilities. *International Journal for Numerical Methods in Engineering* 79(11), pp. 1309-1331, 2009.
- [17] Hesthaven, Jan S., and Tim Warburton. *Nodal discontinuous Galerkin methods: algorithms, analysis, and applications*. Vol. 54. Springer, 2008.
- [18] Tu, Shuangzhang, and Shahrouz Aliabadi. "A slope limiting procedure in discontinuous Galerkin finite element method for gasdynamics applications." *International Journal of Numerical Analysis and Modeling* 2.2 (2005): 163-178.
- [19] Finio, B. M., N. O. Pérez-Arancibia, and R. J. Wood. "System identification, modeling, and optimization of an insect-sized flapping-wing micro air vehicle." submitted to IEEE/RSJ Int. Conf. Intell. Robots Syst., San Francisco, CA. 2011.
- [20] R. Malka, A.L. Desbiens, Y. Chen, and R.J. Wood, *IEEE/RSJ Int. Conf. on Intelligent Robots and Systems*, Chicago, IL, Sept. 2014.
- [21] Sane, Sanjay P., and Michael H. Dickinson. "The control of flight force by a flapping-wing: lift and drag production." *Journal of experimental biology* 204.15 (2001): 2607-2626.